Check for updates

RESEARCH ARTICLE OPEN ACCESS

$NiMoO_4$ With High Oxidation States for Efficient Electrooxidation of Amines to Nitriles

Hao Chen[1] | Man Qiao[2] | Zhixiang Yuan[1] | Dazhi Yao[3] | Dongdong Zhu[2] | Ping Chen[1]

[1]School of Materials Science and Engineering, Anhui University, Hefei, Anhui, China | [2]School of Chemistry and Materials Science, Jiangsu Key Laboratory of New Energy Devices and Interface Science, Nanjing University of Information Science and Technology, Nanjing, China | [3]School of Chemistry, The University of New South Wales, Sydney, New South Wales, Australia

Correspondence: Dongdong Zhu (dd.zhu@nuist.edu.cn) | Ping Chen (chenping@ahu.edu.cn)

Received: 21 September 2024 | **Revised:** 25 May 2025 | **Accepted:** 27 May 2025

Keywords: amine electrooxidation | electrocatalysis | $NiMoO_4$ | nitrile | oxidation state modulation

ABSTRACT

Electrochemical oxidation of amines to nitriles, with water as the O source, is a green and sustainable route to synthesize nitriles under mild conditions. However, developing highly efficient electrocatalysts for amine oxidation with large current densities is quite challenging. Herein, it is demonstrated that $NiMoO_4$ with high oxidation states can efficiently catalyze benzylamine oxidation reaction (BAOR) to benzonitrile (BN) with a large anodic current density of 300.0 mA cm^{-2} at 1.47 V versus RHE. Impressively, $NiMoO_4$ simultaneously achieves high BA conversion, BN selectivity, and faradaic efficiency of BN above 95%, together with a large BN yield of 0.366 mmol h^{-1} at 1.45 V versus RHE. Such excellent performance is also verified in a practical continuous-flow membrane electrode assembly reactor. Electrochemical measurements and in situ techniques uncover that NiOOH is the catalytically active species for BAOR, while the generation of NiOOH is more facile and effective on $NiMoO_4$ than on $Ni(OH)_2$. Theoretical calculations reveal that Mo doping in NiOOH facilitates the adsorption of BA, and reduces the energy barriers for the subsequent dehydrogenation steps, leading to excellent BAOR performance.

1 | Introduction

Water electrolysis with renewable electricity has been regarded as a promising and sustainable way to produce green hydrogen [1–5]. In fact, by using water as an H or O source, electrochemical hydrogenation or oxidation of molecules offers a safe and efficient approach to synthesize hydrogenated or oxidized products under ambient conditions [6–9]. Nitriles, with a −C≡N functional group, are an important class of organic compounds with widespread applications in pharmaceuticals, agrochemicals, and fine chemicals [10–12]. At present, industrial-scale production of nitriles is dominated by hydrocyanation and ammoxidation. Hydrocyanation involves nucleophilic substitution reactions between alkenes and cyanide, which is highly toxic [13, 14]. Ammoxidation is more favorable, but it still requires the use of strong oxidants at high temperatures, resulting in safety concerns and high energy consumption [15]. Therefore, it is highly desirable to develop a green and energy-efficient way to achieve mass production of nitriles under mild conditions. Recent advances reveal that electrochemical oxidation of amines ($-CH_2NH_2$) is an appealing way to synthesize nitriles, and such a dehydrogenation process is accomplished by using water as the green oxygen source [16]. The obtained nitrile product is easy to separate from the electrolyte owing to its hydrophobic property, thus avoiding the possible overoxidation of nitrile to achieve high selectivity [17]. Moreover, energy-saving hydrogen

Hao Chen and Man Qiao contributed equally to this work.

This is an open access article under the terms of the Creative Commons Attribution License, which permits use, distribution and reproduction in any medium, provided the original work is properly cited.

© 2026 The Author(s). *Exploration* published by Henan University and John Wiley & Sons Australia, Ltd.

production can be realized via using electrochemical oxidation of amines to replace the traditional oxygen evolution reaction at the anode of an electrolyzer, due to its intrinsic thermodynamic advantage [18].

Electrochemical oxidation of amines to nitriles is a complicated four-electron transfer process with multiple steps, and it is imperative to develop highly active and selective electrocatalysts to promote this kinetically sluggish process [19]. Recently, some inspiring works have been reported in this emerging research area. Guo et al. found that $CoSe_2$ with Se vacancies and Ni substitutions can efficiently oxidize benzylamine (BA) to benzonitrile (BN), and the current density for benzylamine oxidation reaction (BAOR) at 1.5 V (vs. reversible hydrogen electrode, RHE) is 120.0 mA cm^{-2} [20]. Zhai and co-workers constructed vacancy-rich $Ni(OH)_2$ nanosheets for propylamine electrooxidation, and obtained anodic current density at 1.41 V versus RHE is 50.0 mA cm^{-2} [21]. Zhao et al. prepared Fe doped Ni_3S_2 electrocatalyst towards BAOR, and the current density at 1.5 V versus RHE is less than 90.0 mA cm^{-2} [22]. Chen and co-workers reported that Ru-modified Ni_2P nanobelt electrode can selectively oxidize BA to BN, and a BAOR current density of 100.0 mA cm^{-2} was attained at 1.4 V versus RHE [14]. In spite of these significant achievements, there is still much room for the catalyst performance improvement. For instance, the currently reported electrocatalysts for amine electrooxidation only show moderate catalytic activity, as the anodic current densities are generally below 300 mA cm^{-2} at 1.5 V versus RHE [23–25]. Moreover, the underlying reaction mechanism of amine electrooxidation needs to be further explored.

Herein, $NiMoO_4$ catalyst with high oxidation states was prepared on nickel foam (NF) for BAOR, which affords a large anodic current density of 300.0 mA cm^{-2} at 1.47 V versus RHE. The as-fabricated $NiMoO_4$ shows excellent BAOR performance with high BA conversion, BN selectivity, and faradaic efficiency (FE) of BN above 95% at 1.45 V versus RHE. Moreover, the BN yield of $NiMoO_4$ at 1.45 V versus RHE is 0.366 mmol h^{-1}, much higher than that of $Ni(OH)_2$ sample (0.156 mmol h^{-1}). In addition, the $NiMoO_4$ catalyst can stably operate for 30 cycles in a continuous-flow membrane electrode assembly (MEA) electrolyzer. In situ characterizations uncover that $NiMoO_4$ guarantees fast and efficient generation of NiOOH, which is regarded as a catalytically active species for BAOR. Theoretical calculations further demonstrate that the introduction of Mo in NiOOH promotes the adsorption of BA molecules on the catalyst surface and reduces the energy barriers for the following dehydrogenation steps from BA to BN, thus contributing to outstanding BAOR performance.

2 | Results and Discussion

The $NiMoO_4$ catalyst was synthesized on NF by a facile hydrothermal method (see Experimental section for details, and Figure S1, Supporting Information). As shown in Figure 1a, except for three sharp peaks stemmed from the NF substrate, the X-ray diffraction (XRD) pattern of the obtained sample is well indexed to $NiMoO_4{\cdot}0.7H_2O$ (JCPDS No. 97-024-7435) [26, 27]. Therefore, for simplicity, the obtained catalyst is named $NiMoO_4$. The scanning electron microscopy (SEM) images (Figure 1b and Figure S2, Supporting Information) display that the $NiMoO_4$ microspheres are covered on the NF substrate, and nanosheets can be observed on the surface of these $NiMoO_4$ microspheres. However, when sodium laurylsulfonate was not used during the hydrothermal process, the morphology of the obtained $NiMoO_4$ sample completely changed, with dense and irregular nanorods generated on the NF substrate (Figure S3, Supporting Information). The high-resolution transmission electron microscopy (HRTEM) image in Figure 1c exhibits clear lattice fringes with an interplanar distance of 0.324 nm, which corresponds well to the (020) plane of $NiMoO_4{\cdot}0.7H_2O$, again confirming the successful preparation of $NiMoO_4$. The high-angle annular dark-field scanning TEM (HAADF-STEM) image, and corresponding elemental mapping results of $NiMoO_4$ (Figure S4, Supporting Information) reveal the uniform distribution of Ni, Mo, and O elements. For comparison, a typical nickel-based catalyst, $Ni(OH)_2$ was also prepared (Figure S5, Supporting Information). The N_2 adsorption–desorption isotherms (Figure S6, Supporting Information) show that the Brunauer–Emmett–Teller (BET) surface area of $NiMoO_4$ (288.37 m^2 g^{-1}) exceeds that of $Ni(OH)_2$ (111.54 m^2 g^{-1}). X-ray photoelectron spectroscopy (XPS) survey spectrum of $NiMoO_4$ verifies the coexistence of Ni, Mo, and O elements (Figure S7, Supporting Information). Notably, as displayed in Figure 1d, compared to $Ni(OH)_2$ sample, all the Ni 2p peaks of $NiMoO_4$ shift noticeably to higher binding energy regions, suggesting a higher oxidation state of Ni cations in $NiMoO_4$. The fitted Ni 2p spectra of $NiMoO_4$ and $Ni(OH)_2$ (Figure S8, Supporting Information) also confirm that $NiMoO_4$ has a higher content of Ni^{3+} species than that of $Ni(OH)_2$. The Mo 3d spectrum of $NiMoO_4$ in Figure 1e shows two main peaks positioned at 235.5 and 232.4 eV, which correspond well to Mo^{6+} $3d_{3/2}$, and Mo^{6+} $3d_{5/2}$, respectively [28, 29]. The XPS O 1s spectrum of $NiMoO_4$ (Figure S9, Supporting Information) exhibits two peaks at 530.7, and 533.0 eV, well assigned to metal–O (M-O) bond, and O−H bond from surface water [30]. X-ray absorption spectroscopy (XAS) was further applied to investigate the chemical state and local coordination environment of the samples. The Ni K-edge X-ray absorption near-edge structure (XANES) spectra of $NiMoO_4$, $Ni(OH)_2$, and Ni foil are presented in Figure 1f. Compared to $Ni(OH)_2$, the absorption edge of $NiMoO_4$ moves to higher energy regions, confirming the higher oxidation state of Ni cations in $NiMoO_4$, which aligns with previous XPS results. Fourier transform k^3-weighted extended X-ray absorption fine structure (FT-EXAFS) spectra of the samples are displayed in Figure 1g. Notably, for $NiMoO_4$, the prominent peak at ≈1.6 Å is attributed to Ni-O coordination in the first shell, while the peak appeared at ≈2.7 Å is assigned to Ni-O-Ni/Mo (Ni-Ni/Mo) coordination in the second shell [31–33]. The presence of Ni-O-Ni/Mo in $NiMoO_4$ is further corroborated by wavelet transform (WT)-EXAFS analysis. The WT contour plots of $Ni(OH)_2$ in Figure 1h exhibit a sharp zone ($R = 2.7$ Å and $k = 7.5$ $Å^{-1}$), which is attributed to the Ni-O-Ni coordination. In contrast, as displayed in Figure 1i, $NiMoO_4$ has a distinct k value greater than 7.5 $Å^{-1}$, indicating the presence of Ni-O-Ni/Mo rather than Ni-O-Ni in the second shell for $NiMoO_4$. In conclusion, all the results above clearly demonstrate that $NiMoO_4$ with high oxidation states was successfully prepared.

To evaluate the catalytic performance of the as-synthesized $NiMoO_4$, a series of electrochemical measurements was carried out using a three-electrode configuration in a two-chambered H-type electrolytic cell first. Figure 2a shows the linear sweep voltammetry (LSV) curves of $NiMoO_4$ in different electrolytes.

27662098, 2026, 1, Downloaded from https://onlinelibrary.wiley.com/doi/10.1002/EXP.20240327 by CochraneChina, Wiley Online Library on [08/06/2026]. See the Terms and Conditions (https://onlinelibrary.wiley.com/terms-and-conditions) on Wiley Online Library for rules of use; OA articles are governed by the applicable Creative Commons License

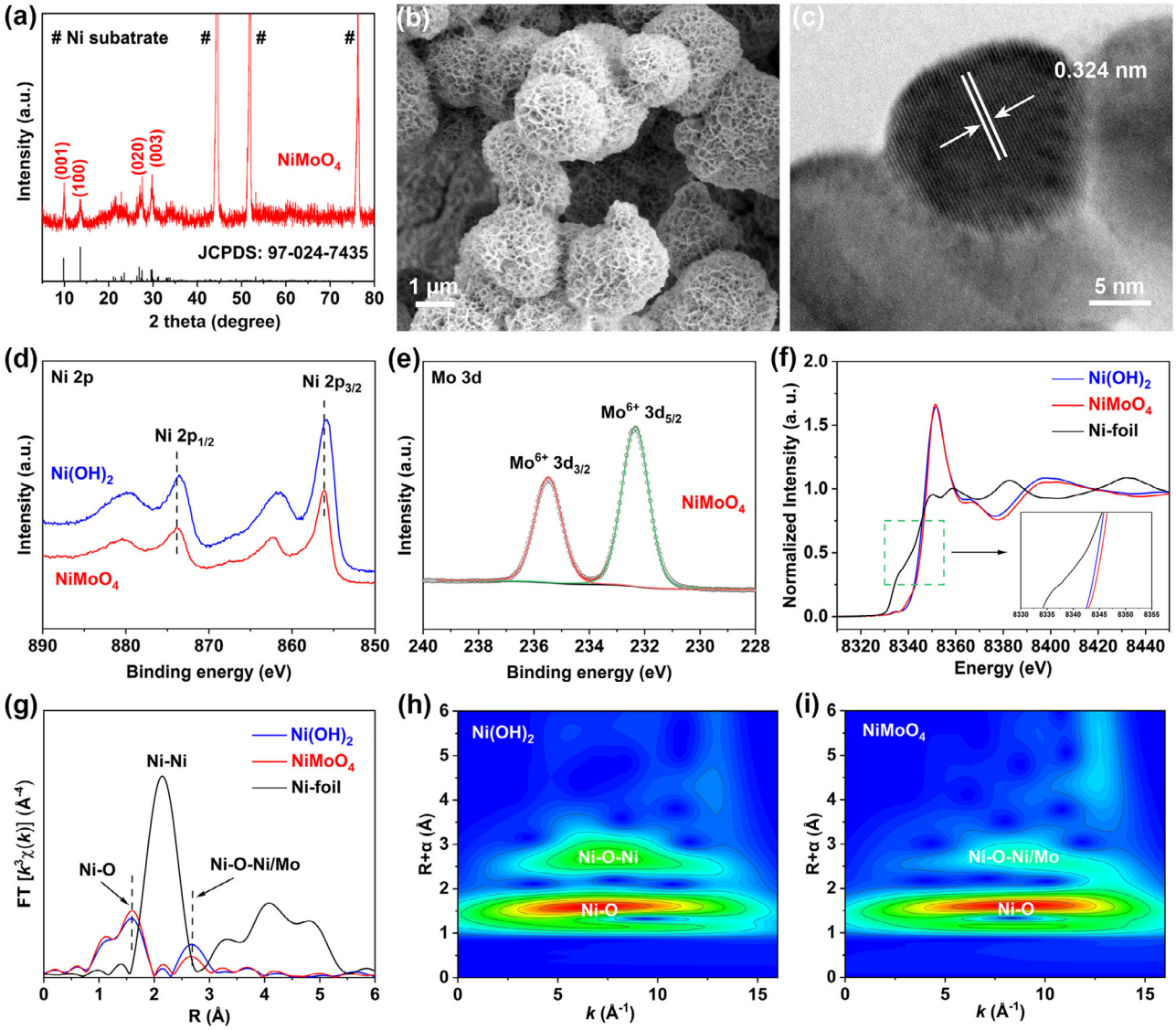


FIGURE 1 | (a) XRD pattern of $NiMoO_4$. (b) SEM image of $NiMoO_4$. (c) HRTEM image of $NiMoO_4$. (d) XPS Ni 2p spectra of $Ni(OH)_2$ and $NiMoO_4$. (e) XPS Mo 3d spectrum of $NiMoO_4$. (f) Ni K-edge XANES spectra of $Ni(OH)_2$, $NiMoO_4$, and Ni foil. (g) Ni K-edge FT-EXAFS spectra of $Ni(OH)_2$, $NiMoO_4$, and Ni foil. WT-EXAFS contour plots of (h) $Ni(OH)_2$, and (i) $NiMoO_4$.

It is worth noting that 90%*iR compensation is applied to the LSV curves. When performed in 1.0 M KOH, there is a significant oxidation peak at around 1.36 V versus RHE, which is attributed to the oxidation of Ni^{2+} to Ni^{3+} species [34, 35]. Afterward, OER starts with a high onset potential of 1.47 V versus RHE. After the addition of 10.0 mM BA, $NiMoO_4$ exhibits a low onset potential of 1.3 V versus RHE toward BAOR, together with greatly enhanced anodic current densities. Herein, such an onset potential advantage means that by choosing a suitable applied potential, the competing OER can be completely avoided during BAOR. It is generally accepted that for Ni-based catalysts, the in situ formed NiOOH species provides catalytically active sites for amine oxidation reactions, including BAOR [36, 37]. Therefore, fast and efficient generation of NiOOH species is critical for achieving outstanding BAOR performance. As exhibited in Figure 2b, $NiMoO_4$ has a much lower onset potential for Ni^{2+} oxidation to Ni^{3+} than that of $Ni(OH)_2$, accompanied by a greatly increased oxidation peak area, indicating that the generation of active NiOOH species is more facile on $NiMoO_4$. Not surprisingly, compared to $Ni(OH)_2$, $NiMoO_4$ shows a lower onset potential and higher current densities toward BAOR (Figure 2c). For instance, at 1.47 V versus RHE, $NiMoO_4$ achieves an industrial current density of 300.0 mA cm^{-2}, while the current density for $Ni(OH)_2$ is only 164.7 mA cm^{-2}. The bare NF was also tested for BAOR, while its poor catalytic performance confirms that the intrinsic catalytic activity for BAOR originates from the $NiMoO_4$ catalyst, rather than the NF substrate (Figure S10, Supporting Information). $NiMoO_4$ also possesses much higher current densities toward BAOR than commercial RuO_2. In fact, such exceptional BAOR performance of $NiMoO_4$ has rarely been reported before (Table S1, Supporting Information). Moreover, $NiMoO_4$ has a larger double-layer capacitance (C_{dl}) value than that of $Ni(OH)_2$ (Figure S11, Supporting Information), suggesting that $NiMoO_4$ with a larger electrochemically active surface area can provide more catalytically active sites toward BAOR, contributing to its improved BAOR activity. In Figure 2d, the Tafel slope of

27662098, 2026, 1, Downloaded from https://onlinelibrary.wiley.com/doi/10.1002/EXP.20240327 by CochraneChina, Wiley Online Library on [08/06/2026]. See the Terms and Conditions (https://onlinelibrary.wiley.com/terms-and-conditions) on Wiley Online Library for rules of use; OA articles are governed by the applicable Creative Commons License

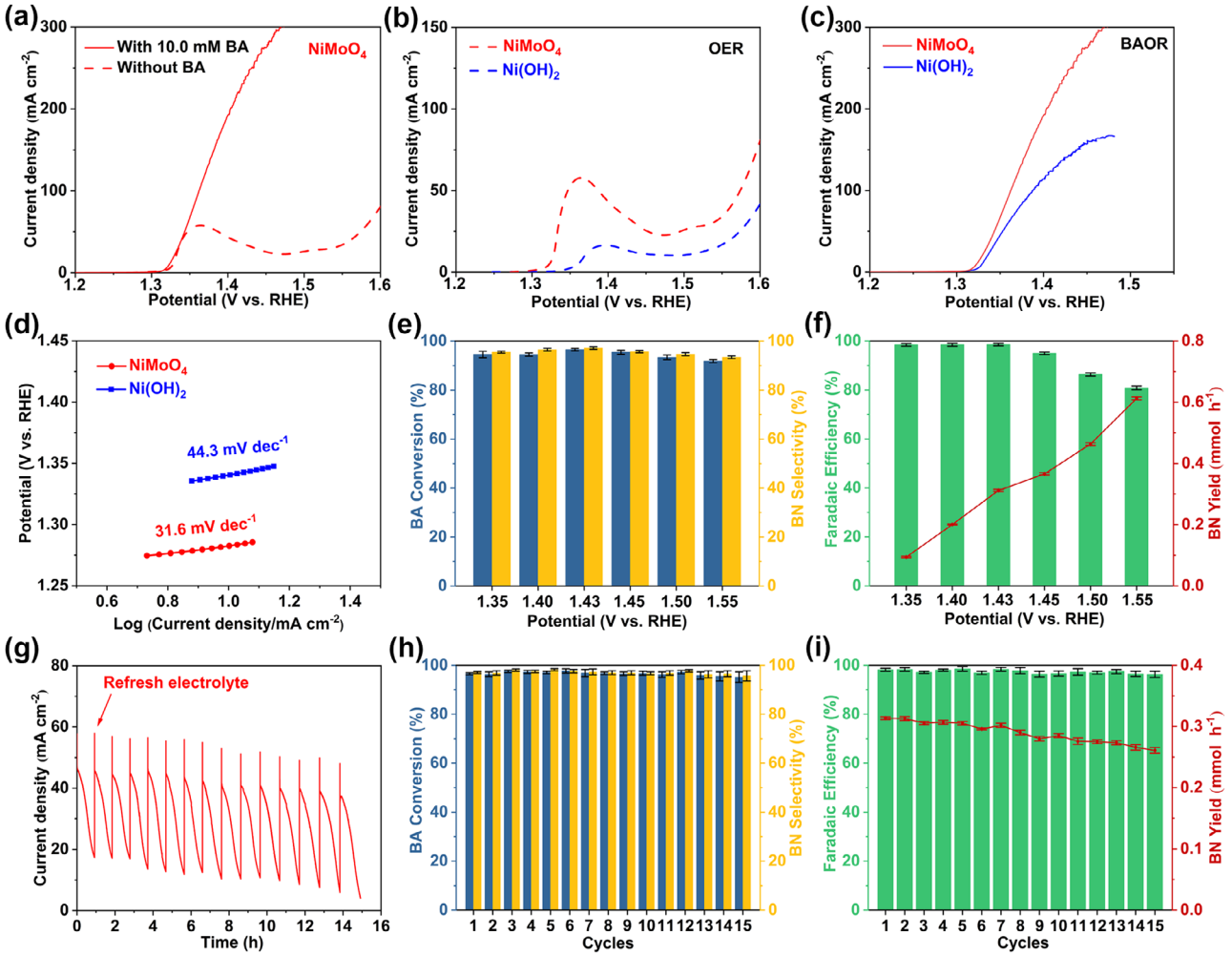


FIGURE 2 | (a) LSV curves of $NiMoO_4$ in 1.0 M KOH with or without 10.0 mM BA. (b) LSV curves of $NiMoO_4$ and $Ni(OH)_2$ in 1.0 M KOH. (c) LSV curves of $NiMoO_4$ and $Ni(OH)_2$ in 1.0 M KOH with 10.0 mM BA. (d) Tafel plots of $NiMoO_4$ and $Ni(OH)_2$. (e) BA conversion, and BN selectivity of $NiMoO_4$ at various potentials. (f) FE of BN and BN yield of $NiMoO_4$ at various potentials. (g) The successive chronoamperometry test of $NiMoO_4$ at 1.43 V versus RHE for 15 cycles. (h) BA conversion, and BN selectivity of $NiMoO_4$ for 15 cycles. (i) FE of BN, and BN yield of $NiMoO_4$ for 15 cycles.

$NiMoO_4$ is smaller (31.6 mV dec^{-1}) than that of $Ni(OH)_2$ (44.3 mV dec^{-1}), implying a more favorable reaction kinetics of $NiMoO_4$ toward BAOR. To investigate the potential dependence of BAOR performance, a chronoamperometry test with the total passing charge of 115.6 C was carried out at different potentials in 1.0 M KOH containing 10.0 mM BA (Figures S12 and S13, Supporting Information). The oil droplets can be clearly observed on the surface of the electrolyte after BAOR (Figure S14, Supporting Information). The obtained liquid products were measured by a gas chromatograph (GC) with calibration curves (Figure S15, Supporting Information). After BAOR with a 30 C passing charge, BN appeared as the product, while the amount of BA substrate reduced (Figure S16, Supporting Information). When 115.6 C was consumed for BAOR, almost all the BA substrate was converted to BN. As shown in Figure 2e, $NiMoO_4$ achieves high BA conversion and BN selectivity above 90% at a wide potential window from 1.35 to 1.55 V versus RHE. The FE of the desired BN is more than 95% when the potential is no higher than 1.45 V versus RHE in Figure 2f. However, due to the competing OER, the FE of BN reduces significantly when the potential is above 1.45 V versus RHE (Figure S17, Supporting Information). Meanwhile, the BN yield increases with the applied more positive potential, and a large BN yield of 0.366 mmol h^{-1} is attained at 1.45 V versus RHE. In contrast, $Ni(OH)_2$ sample achieves reduced FEs of BN, and the BN yield at 1.45 V versus RHE is only 0.156 mmol h^{-1} (Figure S18, Supporting Information). The durability performance of $NiMoO_4$ for BAOR was evaluated by a continuous cycling test for 15 cycles at the potential of 1.43 V versus RHE, and the passing charge for each cycle is 115.6 C (Figure 2g). As depicted in Figure 2h,i, though the reaction rate of BAOR is slightly influenced, $NiMoO_4$ presents good BAOR stability with no obvious attenuation of BA conversion, BN selectivity, or FE of BN during the 15-cycle test. The BAOR stability performance of $Ni(OH)_2$ was also investigated (Figure S19 and S20, Supporting Information), and the BN yield on $Ni(OH)_2$ is much lower than that of $NiMoO_4$ at each cycle. To explore the BAOR performance of $NiMoO_4$ in low alkaline medium, we carried out the test in 0.1 M KOH/0.5 M Na_2SO_4 with 10.0 mM BA (Figure S21, Supporting Information). The obtained results clearly show that $NiMoO_4$ is still highly efficient for BAOR in low alkaline medium. High BA conversion, BN selectivity, and FE of BN are achieved at a wide potential window from 1.45 to 1.65 V versus RHE. To demonstrate the general applicability of $NiMoO_4$ for amine oxidation to nitrile, cyclohexenylethylamine was chosen as the substrate. The LSV curves show that $NiMoO_4$

27662098, 2026, 1, Downloaded from https://onlinelibrary.wiley.com/doi/10.1002/EXP.20240327 by CochraneChina, Wiley Online Library on [08/06/2026]. See the Terms and Conditions (https://onlinelibrary.wiley.com/terms-and-conditions) on Wiley Online Library for rules of use; OA articles are governed by the applicable Creative Commons License

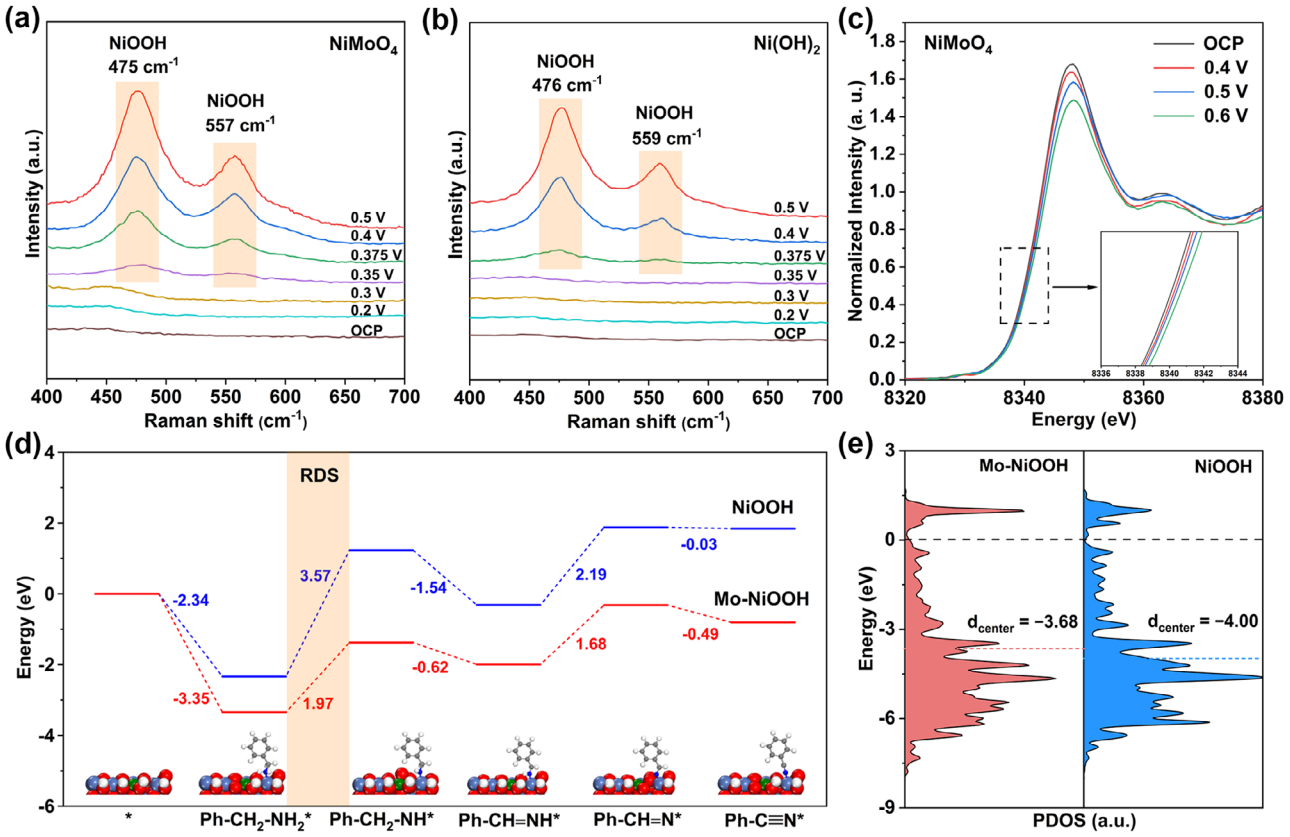


FIGURE 3 | (a) Potential-dependent in situ Raman spectra of $NiMoO_4$ electrode collected in 1.0 M KOH with 10.0 mM BA. (b) Potential-dependent in situ Raman spectra of $Ni(OH)_2$ electrode collected in 1.0 M KOH with 10.0 mM BA. (c) In situ Ni K-edge XANES spectra of $NiMoO_4$ electrode during the BAOR process. (d) Free energy diagrams for BAOR and corresponding intermediate adsorption on Mo-NiOOH and NiOOH. (e) PDOS of Mo-NiOOH and NiOOH.

is highly active for cyclohexenylethylamine oxidation (Figure S22, Supporting Information). When the applied potential is no higher than 1.45 V versus RHE, large amine conversion, nitrile selectivity, and FE of nitrile above 90% are attained, highlighting the great potential of $NiMoO_4$ electrode for other amine oxidation reactions.

To probe the structure evolution of the catalysts during BAOR, in situ techniques were applied. As shown in Figure 3a, in situ Raman spectra of $NiMoO_4$ show that when the potential increases to 0.35 V versus Ag/AgCl, two distinct peaks at 475 and 557 cm^{-1} appear, which are well assigned to β-NiOOH [38]. However, for $Ni(OH)_2$, NiOOH can only be observed when the potential is no less than 0.375 V versus Ag/AgCl (Figure 3b), giving strong evidence that the generation of active NiOOH species is more facile on $NiMoO_4$. Moreover, when the reaction time increases from 30 to 600 s (Figure S23, Supporting Information), the Raman peak intensity is gradually enhanced, revealing the formation of more NiOOH species. In situ Ni K-edge XANES spectra in Figure 3c uncover that BAOR on $NiMoO_4$ is closely associated with the oxidation state change of Ni cations. In detail, the oxidation state of Ni increases with the applied more positive potential, indicating that the in situ formed high-valence Ni species provides catalytically active sites for BAOR. Density functional theory (DFT) calculations were further carried out to elucidate the underlying mechanism of BAOR. Based on the experimental findings that the in situ generated NiOOH species is the real catalytically active species for BAOR, the constructed structural models for $NiMoO_4$ and $Ni(OH)_2$ catalysts are Mo-NiOOH and NiOOH, respectively (see Experimental Section for computational details, and Figure S24, Supporting Information). The reaction pathway and energy diagrams for BAOR to BN on NiOOH and Mo-NiOOH models are presented in Figure 3d. The BAOR initials with the adsorption of BA, and the adsorption energy ($Ph-CH_2-NH_2^*$) is calculated to be −2.34 and −3.35 eV for NiOOH and Mo-NiOOH, respectively. The relatively strong adsorption of BA on Mo-NiOOH is desirable for BA activation for the subsequent oxidation reaction. Afterward, BAOR proceeds with continuous dehydrogenation steps: $Ph-CH_2-NH_2^* \rightarrow Ph-CH_2-NH^* \rightarrow Ph-CH=NH^* \rightarrow Ph-CH=N^* \rightarrow Ph-C\equiv N^*$. The rate-determining step (RDS) of the entire BAOR is the first dehydrogenation step, which forms the $Ph-CH_2-NH^*$ intermediate. The energy barrier of this RDS is 1.97 eV for Mo-NiOOH, which is much smaller than that of NiOOH (3.57 eV), demonstrating that Mo incorporation promotes BAOR. The enhanced adsorption of BA can be reflected by the electronic interaction between the catalyst and BA [39]. Charge density difference calculation (Figure S24, Supporting Information) shows that Mo-NiOOH gains 0.34 $|e^-|$ from the BA molecule, while only 0.15 $|e^-|$ transfers to NiOOH. It is well suspected that highly oxidized Ni in Mo-NiOOH is electron-deficient, which is beneficial for the adsorption of BA by attracting the lone pair electrons from its amine group ($-NH_2$) [21]. Moreover, projected density of state (PDOS) was used to reflect the change of the d-band center (ε_d).

27662098, 2026, 1, Downloaded from https://onlinelibrary.wiley.com/doi/10.1002/EXP.20240327 by CochraneChina, Wiley Online Library on [08/06/2026]. See the Terms and Conditions (https://onlinelibrary.wiley.com/terms-and-conditions) on Wiley Online Library for rules of use; OA articles are governed by the applicable Creative Commons License

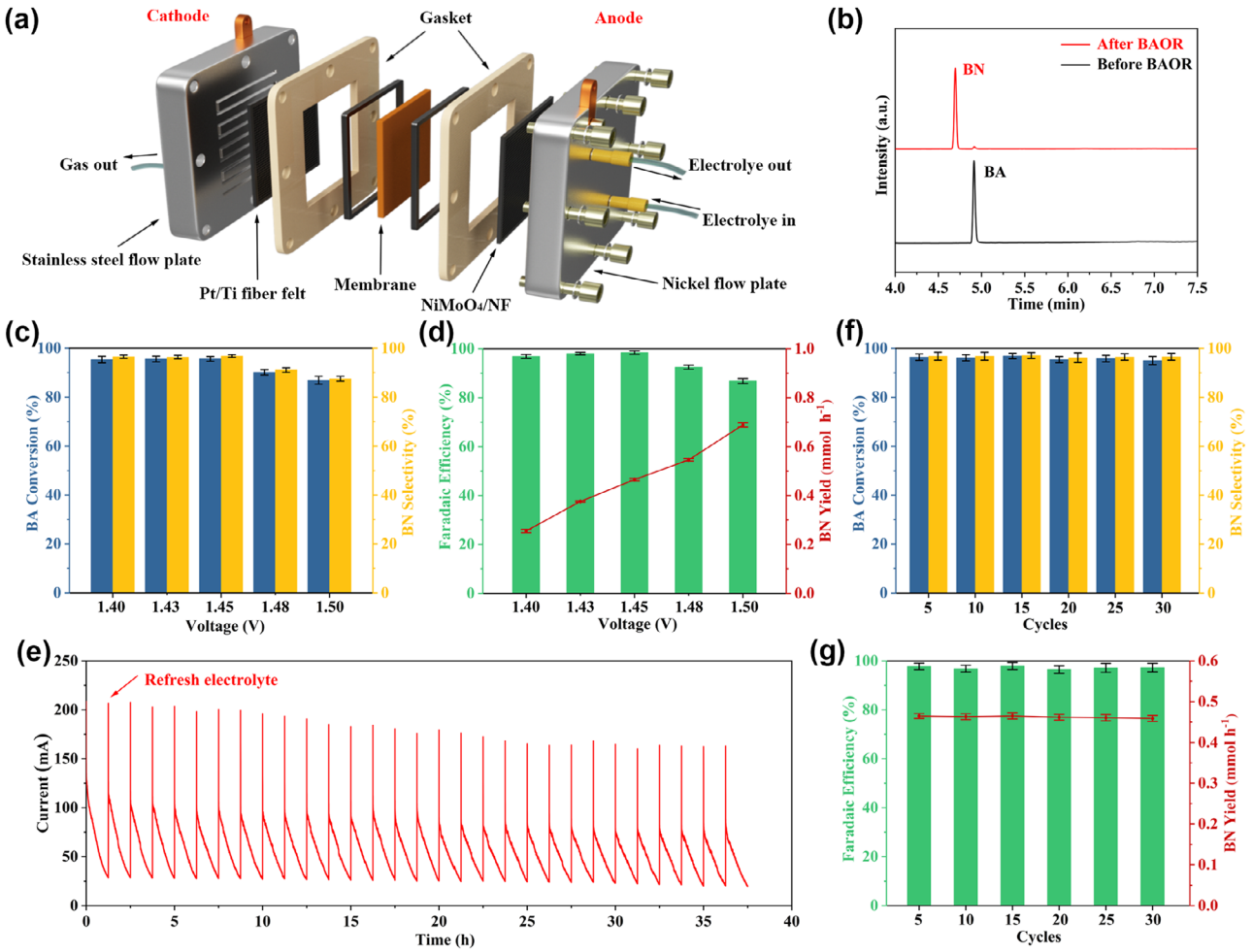


FIGURE 4 | (a) Schematic diagram of a continuous-flow MEA reactor. (b) Detection of the anode product after BAOR. (c) BA conversion, and BN selectivity at different cell voltages. (d) FE of BN, and BN yield at different cell voltages. (e) Stability test with a constant cell voltage of 1.45 V for 30 cycles. (f) BA conversion, and BN selectivity during the stability test. (g) FE of BN, and BN yield during the stability test.

As shown in Figure 3e, the ε_d of Mo-NiOOH (−3.68 eV) is closer to the Fermi level (E_f) than that of NiOOH (−4.00 eV), indicating that Mo doping in NiOOH leads to the upshift of ε_d, which raises the antibonding level, contributing to enhanced BA adsorption [40, 41]. Overall, DFT results indicate that the introduction of Mo in NiOOH is favorable for the chemical adsorption of BA, and subsequent dehydrogenation steps from BA to BN. Moreover, $NiMoO_4$ catalyst can guarantee fast and efficient generation of active Mo-NiOOH species, which is responsible for the excellent BAOR results.

Inspired by the remarkable BAOR performance of $NiMoO_4$ catalyst in the three-electrode system, we further evaluated the performance of $NiMoO_4$ in a more practical scenario. Specifically, as shown in Figure 4a, a continuous-flow MEA reactor using $NiMoO_4$/NF as the anode, and commercial Pt/Ti fiber felt (Figure S25, Supporting Information) as the cathode was constructed for two-electrode tests. Peristaltic pumps were used to drive the electrolyte circulation for supplying raw materials to the electrode surface and quickly removing the products (Figure S26, Supporting Information) [42]. As illustrated in Figure S27, Supporting Information, water is reduced at the cathode to produce hydrogen, while BA is oxidized at the anode. GC was used to detect the liquid product at the anode, and discovered that the product of BA oxidation in this continuous-flow reactor is still BN (Figure 4b). High BA conversion, BN selectivity, and FE of BN beyond 90% are attained under the wide voltage range from 1.4 to 1.48 V (Figure 4c,d). Moreover, a large BN yield of 0.689 mmol h^{-1} was obtained at 1.5 V. The durability behavior of $NiMoO_4$ was investigated by a chronoamperometry test at 1.45 V for 30 cycles (Figure 4e). Impressively, high BA conversion, BN selectivity, and FE of BN above 95% are well retained during the 30 consecutive cycles (Figure 4f,g). In addition, a quite stable and large BN yield of around 0.46 mmol h^{-1} was achieved during the whole stability test. To uncover the possible change of the catalyst during BAOR, a series of characterizations was performed after the cycling test. XRD patterns show that, besides $NiMoO_4$, NiOOH emerges after the BAOR cycling test (Figure S28a, Supporting Information). Moreover, characteristic peaks assigned to NiOOH species appear in the Raman spectrum of $NiMoO_4$ after the cycling test, again confirming the generation of NiOOH (Figure S28b, Supporting Information). Ni K-edge XANES spectra (Figure S28c, Supporting Information) also reveal the formation of Ni species with higher oxidation states, in agreement with previous results. SEM image in Figure S28d, Supporting Information, indicates that the original microsphere morphology of $NiMoO_4$

27662098, 2026, 1, Downloaded from https://onlinelibrary.wiley.com/doi/10.1002/EXP.20240327 by CochraneChina, Wiley Online Library on [08/06/2026]. See the Terms and Conditions (https://onlinelibrary.wiley.com/terms-and-conditions) on Wiley Online Library for rules of use; OA articles are governed by the applicable Creative Commons License

is well retained. Thus, it is well suspected that the relatively stable in-situ formed $NiOOH/NiMoO_4$ structure and morphology contribute to the excellent stability performance.

3 | Conclusions

In summary, the $NiMoO_4$ catalyst was successfully prepared by a typical hydrothermal method. XPS and XAS results confirm the higher oxidation states of Ni cations in $NiMoO_4$, compared to $Ni(OH)_2$. The as-synthesized $NiMoO_4$ with high oxidation states shows exceptional performance towards BAOR, and the current density at 1.47 V versus RHE is 300.0 mA cm^{-2}. Specifically, with the applied potential of 1.45 V versus RHE, $NiMoO_4$ achieves high BA conversion, BN selectivity, and FE of BN above 95%, while its BN yield is more than twice higher than that of $Ni(OH)_2$. Moreover, when tested as the anode in a continuous-flow MEA reactor, $NiMoO_4$ displays outstanding BAOR stability with large BN yields of about 0.46 mmol h^{-1} for 30 cycles. Electrochemical method, in situ Raman, and in situ XAS demonstrate that NiOOH is the real active species for BAOR, and its generation is more facile and effective on $NiMoO_4$. DFT calculations clearly show that Mo incorporation in NiOOH facilitates the BA adsorption, and greatly reduces the energy barrier of the rate-determining step (formation of $Ph{-}CH_2{-}NH^*$ intermediate) from 3.57 to 1.97 eV, thus contributing to the excellent BAOR performance. This work not only provides a highly efficient and stable electrocatalyst for BAOR but also highlights the importance of oxidation state modulation in the electrocatalyst design for organic oxidation reactions.

Acknowledgments

The authors gratefully acknowledge the financial support by the National Natural Science Foundation of China (22275001, 22203045, 22402084), Project of Anhui Provincial Department of Education (2022AH010004, KJ2021ZD0002), and China Postdoctoral Science Foundation (2023M741771). We acknowledge the High Performance Computing Center of Nanjing University of Information Science & Technology for their support of this work.

Conflicts of Interest

The authors declare no conflicts of interest.

Data Availability Statement

The data that support the findings of this study are available from the corresponding author upon reasonable request.

References

1. S.-K. Geng, Y. Zheng, S.-Q. Li, et al., "Nickel Ferrocyanide as a High-Performance Urea Oxidation Electrocatalyst," *Nature Energy* 6 (2021): 904–912.

2. T. Wang, X. Cao, and L. Jiao, "Progress in Hydrogen Production Coupled With Electrochemical Oxidation of Small Molecules," *Angewandte Chemie International Edition* 61 (2022): e202213328.

3. H. Jin, X. Liu, P. An, et al., "Dynamic Rhenium Dopant Boosts Ruthenium Oxide for Durable Oxygen Evolution," *Nature Communications* 14 (2023): 354.

4. Y. Hu, L. Shao, Z. Jiang, et al., "Unveiling the Role of Boron on Nickel-Based Catalyst for Efficient Urea Oxidation Assisted Hydrogen Production," *Advanced Functional Materials* 34 (2024): 2411011.

5. N. Wang, S. Song, W. Wu, Z. Deng, and C. Tang, "Bridging Laboratory Electrocatalysts With Industrially Relevant Alkaline Water Electrolyzers," *Advanced Energy Materials* 14 (2024): 2303451.

6. C. Tang, Y. Zheng, M. Jaroniec, and S.-Z. Qiao, "Electrocatalytic Refinery for Sustainable Production of Fuels and Chemicals," *Angewandte Chemie International Edition* 60 (2021): 19572–19590.

7. R. Ge, Y. Wang, Z. Li, et al., "Selective Electrooxidation of Biomass-Derived Alcohols to Aldehydes in a Neutral Medium: Promoted Water Dissociation Over a Nickel-Oxide-Supported Ruthenium Single-Atom Catalyst," *Angewandte Chemie International Edition* 61 (2022): e202200211.

8. W. Xue, L. Quan, H. Liu, et al., "Bromine-Enhanced Generation and Epoxidation of Ethylene in Tandem CO_2 Electrolysis Towards Ethylene Oxide," *Angewandte Chemie International Edition* 62 (2023): e202311570.

9. C. Liu, F. Chen, B.-H. Zhao, Y. Wu, and B. Zhang, "Electrochemical Hydrogenation and Oxidation of Organic Species Involving Water," *Nature Reviews Chemistry* 8 (2024): 277–293.

10. Q. Wen, Y. Lin, Y. Yang, et al., "In Situ Chalcogen Leaching Manipulates Reactant Interface Toward Efficient Amine Electrooxidation," *ACS Nano* 16 (2022): 9572–9582.

11. S. Bai, L. Chen, J. Bai, et al., "V Modified Ni-Based Layer Hydroxides for the Electrocatalytic Upgrading of Amines to Nitriles," *Inorganic Chemistry Frontiers* 10 (2023): 4695–4701.

12. X. Yang, E. Wei, Y. Dong, et al., "Promoting OH* Adsorption by Defect Engineering of CuO Catalysts for Selective Electro-Oxidation of Amines to Nitriles Coupled With Hydrogen Production," *Chemical Science* 15 (2024): 12580–12588.

13. J. C. Reisenbauer, B. N. Bhawal, N. Jelmini, and B. Morandi, "Development of an Operationally Simple, Scalable, and HCN-Free Transfer Hydrocyanation Protocol Using an Air-Stable Nickel Precatalyst," *Organic Process Research & Development* 26 (2022): 1165–1173.

14. X. Liu, X. He, Z. Fang, et al., "Regulating the Local Charge Distribution of Ni Active Sites for Electrosynthesis of Nitriles Coupled With H_2 Production," *Chemistry of Materials* 36 (2024): 968–979.

15. Y. Sun, H. Shin, F. Wang, et al., "Highly Selective Electrocatalytic Oxidation of Amines to Nitriles Assisted by Water Oxidation on Metal-Doped α-$Ni(OH)_2$," *Journal of the American Chemical Society* 144 (2022): 15185–15192.

16. Y. Liu, Z. Yang, Y. Zou, S. Wang, and J. He, "Interfacial Micro-Environment of Electrocatalysis and Its Applications for Organic Electro-Oxidation Reaction," *Small* 20 (2024): 2306488.

17. K. Chen, W. Zhang, Y. Bai, et al., "Boosting Electrochemical Hydrogen Evolution by Coupling Anodically Oxidative Dehydrogenation of Benzylamine to Benzonitrile," *Chinese Chemical Letters* 34 (2023): 107319.

18. Y. Li, Y. Jiao, H. Yan, et al., "Mo–Ni-based Heterojunction With Fine-customized d-Band Centers for Hydrogen Production Coupled With Benzylamine Electrooxidation in Low Alkaline Medium," *Angewandte Chemie International Edition* 62 (2023): e202306640.

19. Y. Huang, X. Chong, C. Liu, Y. Liang, and B. Zhang, "Boosting Hydrogen Production by Anodic Oxidation of Primary Amines Over a NiSe Nanorod Electrode," *Angewandte Chemie International Edition* 57 (2018): 13163–13166.

20. L. Zeng, W. Chen, Q. Zhang, et al., "$CoSe_2$ Subnanometer Belts With Se Vacancies and Ni Substitutions for the Efficient Electrosynthesis of High-Value-Added Nitriles Coupled With Hydrogen Generation," *ACS Catalysis* 12 (2022): 11391–11401.

21. W. Wang, Y. Wang, R. Yang, et al., "Vacancy-Rich Ni(OH) 2 Drives the Electrooxidation of Amino C–N Bonds to Nitrile C≡N Bonds," *Angewandte Chemie International Edition* 59 (2020): 16974–16981.

27662098, 2026, 1, Downloaded from https://onlinelibrary.wiley.com/doi/10.1002/EXP.20240327 by CochraneChina, Wiley Online Library on [08/06/2026]. See the Terms and Conditions (https://onlinelibrary.wiley.com/terms-and-conditions) on Wiley Online Library for rules of use; OA articles are governed by the applicable Creative Commons License

22. L. Sun, Z. Zhou, Y. Xie, et al., "Surface Self-Reconstruction of Fe-Ni_3S_2 Electrocatalyst for Value-Generating Nitrile Evolution Reaction to Drive Efficient Hydrogen Production," *Advanced Functional Materials* 33 (2023): 2301884.

23. Y. Ding, B.-Q. Miao, S.-N. Li, et al., "Benzylamine Oxidation Boosted Electrochemical Water-Splitting: Hydrogen and Benzonitrile Co-Production at Ultra-Thin Ni_2P Nanomeshes Grown on Nickel Foam," *Applied Catalysis B* 268 (2020): 118393.

24. X. Pan, L. Sun, Z. Zhou, et al., "Positive Electronic Nickel Active Site Enhances N—H/C—H Bonds Breaking for Electrooxidation of Amines to Nitriles Coupling With Hydrogen Production," *Advanced Energy Materials* 14 (2024): 2400374.

25. Z. Tu, X. He, X. Liu, et al., "Electronic Modification of Ni Active Sites by W for Selective Benzylamine Oxidation and Concurrent Hydrogen Production," *Chinese Journal of Catalysis* 58 (2024): 146–156.

26. J. Lu, S. Chen, Y. Zhuo, X. Mao, D. Liu, and Z. Wang, "Greatly Boosting Seawater Hydrogen Evolution by Surface Amorphization and Morphology Engineering on $MoO_2/Ni_3(PO_4)_2$," *Advanced Functional Materials* 33 (2023): 2308191.

27. M. Ning, Y. Wang, L. Wu, et al., "Hierarchical Interconnected NiMoN With Large Specific Surface Area and High Mechanical Strength for Efficient and Stable Alkaline Water/Seawater Hydrogen Evolution," *Nano-Micro Letters* 15 (2023): 157.

28. Q. Zhang, W. Xiao, W. H. Guo, et al., "Macroporous Array Induced Multiscale Modulation at the Surface/Interface of Co(OH) 2 /NiMo Self-Supporting Electrode for Effective Overall Water Splitting," *Advanced Functional Materials* 31 (2021): 2102117.

29. P. Xue, M. Qiao, J. Miao, Y. Tang, D. Zhu, and C. Guo, "Self-Supported Ru-Doped $NiMoO_4$ for Efficient Hydrogen Evolution With 1000 mA cm^{-2} at a Low Overpotential," *Chemical Communications* 60 (2024): 6423–6426.

30. B. Li, P. Xue, Y. Bai, Q. Tang, M. Qiao, and D. Zhu, "Coupling Cu Doping and Oxygen Vacancies in Co_3O_4 for Efficient Electrochemical Nitrate Conversion to Ammonia," *Chemical Communications* 59 (2023): 5086–5089.

31. W.-K. Han, J.-X. Wei, K. Xiao, et al., "Activating Lattice Oxygen in Layered Lithium Oxides Through Cation Vacancies for Enhanced Urea Electrolysis," *Angewandte Chemie International Edition* 61 (2022): e202206050.

32. X. Zheng, J. Yang, P. Li, et al., "Dual-Atom Support Boosts Nickel-Catalyzed Urea Electrooxidation," *Angewandte Chemie International Edition* 62 (2023): e202217449.

33. J. Wei, H. Tang, Y. Liu, et al., "Optimizing the Intermediates Adsorption by Manipulating the Second Coordination Shell of Ir Single Atoms for Efficient Water Oxidation," *Angewandte Chemie International Edition* 63 (2024): e202410520.

34. D. Zhu, H. Zhang, J. Miao, et al., "Strategies for Designing More Efficient Electrocatalysts Towards the Urea Oxidation Reaction," *Journal of Materials Chemistry A* 10 (2022): 3296–3313.

35. R. Lin, L. Kang, T. Zhao, et al., "Identification and Manipulation of Dynamic Active Site Deficiency-Induced Competing Reactions in Electrocatalytic Oxidation Processes," *Energy & Environmental Science* 15 (2022): 2386–2396.

36. M. T. Bender and K.-S. Choi, "Electrochemical Dehydrogenation Pathways of Amines to Nitriles on NiOOH," *JACS Au* 2 (2022): 1169–1180.

37. S. Ghosh, D. Bagchi, I. Mondal, T. Sontheimer, R. V. Jagadeesh, and P. W. Menezes, "Deciphering the Role of Nickel in Electrochemical Organic Oxidation Reactions," *Advanced Energy Materials* 14 (2024): 2400696.

38. C. Johnston and P. R. Graves, "In Situ Raman Spectroscopy Study of the Nickel Oxyhydroxide Electrode (NOE) System," *Applied Spectroscopy* 44 (1990): 105–115.

39. H. Zhang, Q. Yang, S. Luo, et al., "On the Activity and Selectivity of 5-Hydroxymethylfurfural Electrocatalytic Oxidation Over Cation-Defective Nickel Hydroxides," *ACS Catalysis* 14 (2024): 9565–9574.

40. S. Jiao, X. Fu, and H. Huang, "Descriptors for the Evaluation of Electrocatalytic Reactions: D-Band Theory and Beyond," *Advanced Functional Materials* 32 (2022): 2107651.

41. R. Zeng, Q. Gao, L. Xiao, et al., "Precise Tuning of the D-Band Center of Dual-Atomic Enzymes for Catalytic Therapy," *Journal of the American Chemical Society* 146 (2024): 10023–10031.

42. S. Li, S. Wang, Y. Wang, et al., "Doped Mn Enhanced NiS Electrooxidation Performance of HMF Into FDCA at Industrial-Level Current Density," *Advanced Functional Materials* 33 (2023): 2214488.

Supporting Information

Additional supporting information can be found online in the Supporting Information section.

Supporting File 1: exp270133-sup-0001-SuppMat.docx.

27662098, 2026, 1, Downloaded from https://onlinelibrary.wiley.com/doi/10.1002/EXP.20240327 by CochraneChina, Wiley Online Library on [08/06/2026]. See the Terms and Conditions (https://onlinelibrary.wiley.com/terms-and-conditions) on Wiley Online Library for rules of use; OA articles are governed by the applicable Creative Commons License